Dalton Transactions

ROYAL SOCIETY OF CHEMISTRY

PAPER

View Article Online
View Journal | View Issue

Cite this: *Dalton Trans.*, 2025, **54**, 6174

Influence of imidazole functionalization on the properties of small molecule models of the LPMO active site†

Ugo Gilbert,[a] Xiao Mu,[a] Yan Yu Sarah Lam,[a] Gaël De Leener,[b] Martin Schoenauen,[a] Maëlle Bottin,[a] Koen Robeyns,[a] Michel Luhmer,[b] Raphaël Robiette[a] and Michael L. Singleton *[a]

Received 10th December 2024,
Accepted 9th March 2025

DOI: 10.1039/d4dt03424d

rsc.li/dalton

A series of small molecule Cu(II) complexes based on tridentate N_3 ligands relevant to the histidine brace of the active site of lytic polysaccharide monooxygenase were synthesized and characterized by X-ray crystallography and spectroscopic studies. In order to better understand the role of different structural features and to help bridge the differences between previously reported models, the methylation patterns, imidazole connectivity, linker nature, and type of heterocycle were systematically varied across the series. These modifications lead to important differences in the electrochemical properties of the complexes and their reactivity towards the oxidation of a model substrate.

Introduction

Lytic polysaccharide monooxygenases (LPMO) are a family of copper containing metalloenzymes important for biofuel and sustainable commodity chemical production due to their ability to enhance recalcitrant polysaccharide degradation through the oxidative cleavage of strong glycosidic C–H bonds.[1–4] The active site of LPMO consists of a single copper atom bound in a T-shaped N_3 coordination environment, referred to as the histidine brace, which is comprised of the imidazole and primary amine of an N-terminal histidine and a second histidine imidazole, Fig. 1A and B.[5,6] In some members of the LPMO family, the imidazole of the N-terminal histidine is *N*-methylated. The origin and the impact of this modification is still unknown. It has been suggested to protect against oxidative damage, but computational studies suggest it does not impact the mode of action of the histidine brace.[7,8] Further variation in exogenous ligands or second-coordination sphere residues between different LPMO have also been reported.[6,9,10] Still, the core histidine brace is conserved across all members of the LPMO family and this unique arrangement is proposed to be important for the high reactivity of these enzymes. This has made it an intriguing structure for study with synthetic complexes, both to aid in understanding of the structural features important for reactivity and for the possibility to develop new synthetic catalysts capable of similar reactivity.

Nevertheless, despite the apparent simplicity of the histidine brace motif, only a limited number of imidazole containing structural models have been reported so far.[12–25] The Castillo and Simaan groups reported some of the earliest LPMO models using tridentate ligands comprised of either

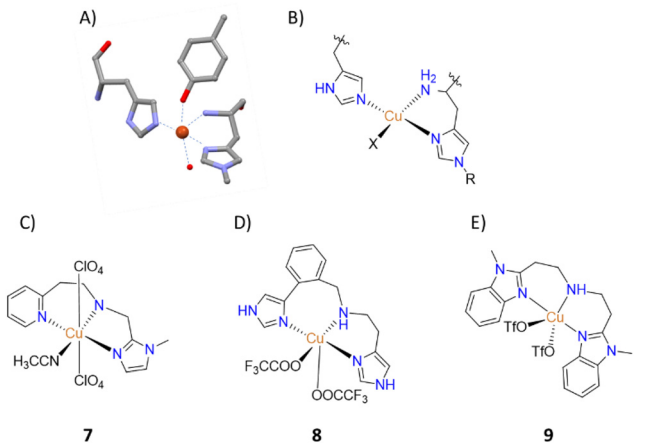

Fig. 1 (A) Structure of the active site of LPMO taken from PDB(4ALC).[11] (B) Schematic structures of the LPMO histidine brace, and reported model complexes (C–E).

[a]*Molecular Chemistry, Materials and Catalysis Division, Institute of Condensed Matter and Nanosciences, Université catholique de Louvain, Place Louis Pasteur 1, Louvain-la-Neuve, 1348, Belgium. E-mail: m.singleton@uclouvain.be*
[b]*Université libre de Bruxelles – ULB, Faculté des Sciences, Laboratoire de Résonance Magnétique Nucléaire Haute Résolution & Centre d'Instrumentation en REsonance Magnétique – CIREM, Avenue F.D. Roosevelt, 50, CP 160/08, 1050 Brussels, Belgium*

† Electronic supplementary information (ESI) available. CCDC 2369751–2369758. For ESI and crystallographic data in CIF or other electronic format see DOI: https://doi.org/10.1039/d4dt03424d

benzimidazoles or one imidazole and one pyridine connected through an aliphatic linker containing a secondary amine (Fig. 1C and E).[26–29] These structures were able to provide a similar N_3 coordination environment as in the natural system and further showed oxidative reactivity towards saccharide substrates in the presence of hydrogen peroxide. Later, Itoh and coworkers, in order to more accurately mimic the imidazoles found in the histidine brace, designed a ligand containing two imidazole rings connected in the 4-position by an alkylamine (Fig. 1D).[30] Their model mimics both the N_3 environment around the copper and better emulates the large dihedral angle between the histidine imidazoles in the enzyme (>50°), a feature they proposed as important for the properties and reactivity of LPMOs. Their system provides not only a good match for the physicochemical properties, in particular the high Cu(II)/Cu(I) reduction potential observed in the natural system but also showed high reactivity toward oxidation of a model saccharide substrate and cyclohexane in presence of hydrogen peroxide making it the best model to date for LPMOs.

Still, structural models of the active site are rare, especially those containing 4- or 5-position connected imidazole units as found in nature, and substantial structural variation (methylation patterns, linker, and heterocycles used) between the reported complexes makes comparison and identification of the effects of different structural features important for the histidine brace reactivity and properties difficult.

In this work, we describe the synthesis, characterization, and reactivity of a series of small molecule copper complexes, (Scheme 1), based on tridentate N_3 ligands composed of two trans imidazoles and an alkylamine linker, mimicking the histidine brace motif of LPMOs. Six new complexes with systematic variation of the imidazole methylation patterns, the connectivity of the imidazole rings, the imine *vs.* amine character of the central N-donor group, and the type of heterocycle present were obtained. Their structures and electrochemical properties were studied along with their oxidative reactivity towards a model saccharide substrate, allowing to demonstrate the impact of different structural modifications on their physicochemical and catalytic properties.

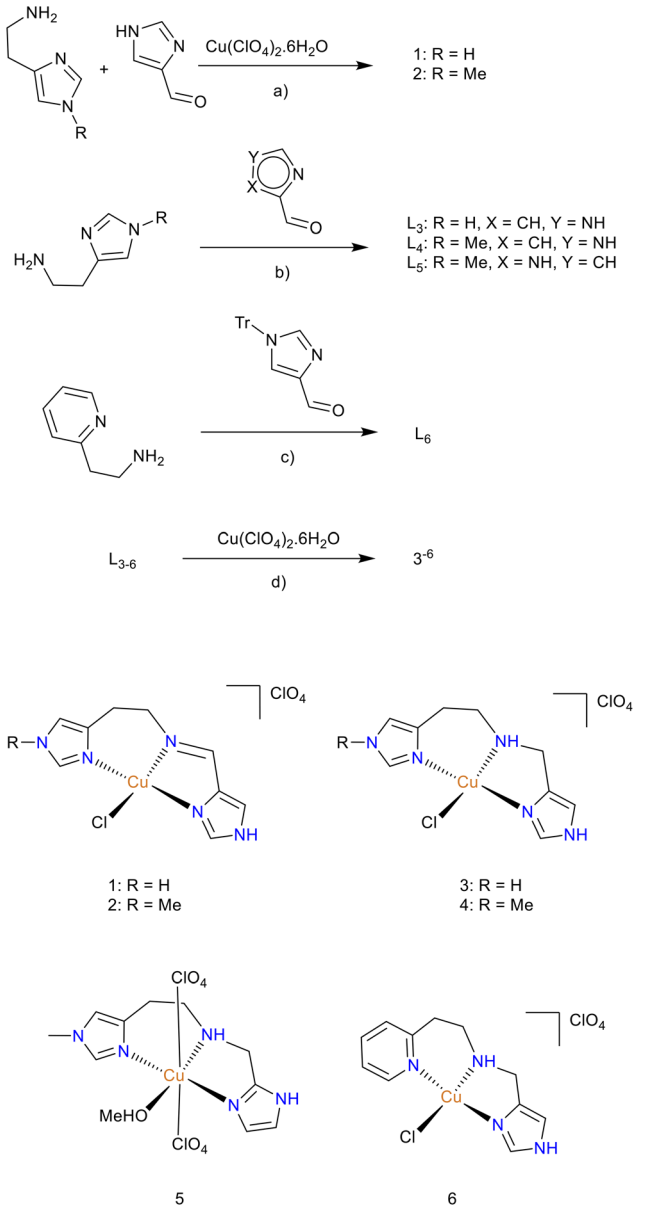

Scheme 1 Synthesis of ligands **L3–6** and complexes **1–6**. (a) MeOH/r.t./overnight. (b) (i) $NaOH/NaBH_4$/MeOH/r.t./4 h, (ii) (if trityl): HCl 35%/r.t./overnight (c) (i): $NaOAc/NaBH_4$/MeOH/r.t./6 h, (ii) HCl 35%/r.t./overnight. (d) MeOH/r.t./overnight.

Results and discussion

Synthetic routes for complexes **1–6** are shown in Scheme 1. The imine complexes **1** and **2** were synthesized in one step through copper templated imine formation by reaction of imidazole-4-carboxaldehyde with the HCl salts of either 1-Me or 1-H histamine in the presence of $Cu(ClO_4)_2$ (**Caution!** Copper perchlorate is a category 2 oxidizing solid and potentially explosive. Precautions should be taken with its handling.) in methanol and isolated by filtration (Schemes 1, S5 and S6†). The amine ligands were synthesized by reductive amination using histamine or 1-methylhistamine[31,32] and imidazole 2-carboxaldehyde or trityl protected imidazole 4-carboxaldehyde[33] in dry methanol in the presence of 3 Å activated molecular sieves (Schemes S1–S4 and S7–S14†). The imine intermediate was observed by NMR but was not isolated due to its low stability. While the direct reduction with sodium borohydride gave **L5** in its neutral form in a good yield, for **L3**, **L4**, and **L6** the tritylated counterpart of the aldehyde was used for the reductive amination to facilitate synthesis and purification. The deprotection of the trityl group was performed quantitatively under aqueous acidic conditions and gave **L3**, **L4**, and **L6** as their HCl salts in moderate to good overall yields.

Complexes **3–6** were then synthesized by adding $Cu(ClO_4)_2$ to a methanol solution of the corresponding ligand followed by precipitation with diethyl ether to give the crude complexes

as blue powders (Schemes S15–S19†). The solids were then purified by crystallization using vapor diffusion of ether into a solution of the complex in methanol to give **3–5** in 20–50% yield.

This crystalline material was used for all analyses. To have a comparison with the literature, complex **7** reported by Simaan and co-workers,[28] containing a pyridine moiety and a 2-position connected imidazole, was resynthesized following the same procedure as for **3–6** (Scheme S20†).

Solid state structures of 1–6

X-ray quality crystals of **1–6** and trityl derivative $\mathbf{3^{Tr}}$ were obtained as described above. The crystal structures are shown in Fig. 2 and important geometric parameters are listed in Table 1. In all cases, the ligands are coordinated to a single Cu center in a tridentate fashion through the two imidazoles and the amine nitrogen of the linker, giving a T-shaped N_3 coordination environment similar to what is observed in LPMO and in previously reported complexes (**7–9**).

Consistent with the elemental analyses, structures **1–4** and **6** contain one free perchlorate counterion and a chloride, originating from the starting HCl salt of the ligand, bound in the fourth equatorial position. By contrast, complex **5**, in which one imidazole is connected to the linker through the 2-position of the ring, has a methanol molecule bound in the equatorial position and two perchlorate counterions, one free and one axially bound, similar to what is described for the complex **7**. The ranges for the $Cu–N_{imid}$ and $Cu–N_{linker}$ distances are 1.92–1.97 Å and 2.04–2.07 Å respectively. The two *cis* $N_{imid}–Cu–N_{linker}$ angles vary expectedly with chelate ring size and measures on average 92.5° on the side of the six-membered chelate ring and 80.4° on the side of the 5-membered chelate ring. Globally, the related pairs of compounds (amine *versus* imine linkers) exhibit nearly identical structural parameters. Notably, the *N*-methylation of the imidazole does not appear to have a substantial impact on the copper structural environment. The same is true for the imidazole connectivity. The distances and angles observed for complex **5** were comparable to the 4-position imidazole derivatives.

Complexes **1**, **2**, and **4** form discrete dimers in the solid state as a result of interactions of the coordinated chlorides with the metal center of a neighboring complex. The average Cu–Cl distances for the equatorially coordinated chloride is 2.3 Å, while the distance to the chloride of the neighboring complex is 2.8 Å, with the Cl–Cu–Cl′ angles ranging between 96–98°. The relatively long distances for the axial chloride interaction suggest that the structures are weakly held together. In related axial chloride bridged copper dimers, dissociation has been shown to occur in protic solvents, with the chlorides being replaced by solvent.[37,38] The weak interaction with chloride is further seen in complex **3**. In contrast to **1**, **2**, and **4**, complex **3** forms extended 1-D coordination polymers in the solid state with longer distances (3.1–3.3 Å) between the copper centers and the neighboring chlorides and a potential hydrogen bonding interaction between the bound chloride and the amine N–H of an adjacent complex. Considering a 5-coordinate N_3ClCl' Cu centre, τ_5 calculated for structures **1–4** is close to 0 (between 0.005 and 0.09), indicating a near perfect square pyramidal arrangement around the copper.[39,40] Like **3**, complex **5** also forms a 1-D coordination polymer. The axially

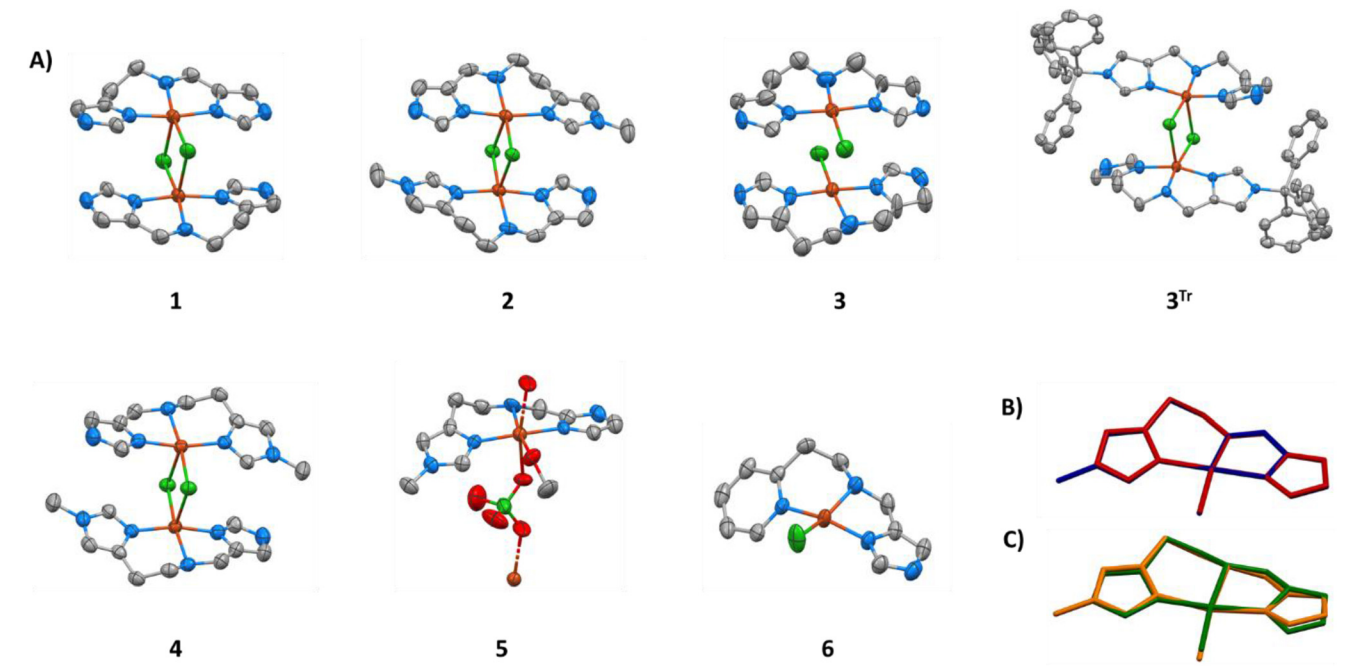

Fig. 2 (A) ORTEP representations of complexes **1–6** and $\mathbf{3^{Tr}}$ with displacement ellipsoids drawn at the 50% occupancy level; hydrogen atoms and non-coordinated perchlorate counterions are omitted for clarity. (B) Overlaid structures of **1** (red) and **2** (blue). (C) Overlaid structures of **3** (green) and **4** (orange).

Table 1 Comparison of the structural properties for compounds **1–7** and LPMO active site

Compound	Cu–N_{imid} (Å)	Cu–N_{linker} (Å)	N–Cu–N_{trans} (°)	N–Cu–N_{cis} (°)	Heterocycle angle[b] (°)
1	1.95	2.04	170.9	91.5, 80.9	15.8
2	1.95, 1.97	2.04	170.4	91.6, 80.8	15.1
3	1.92, 1.9	2.05	174.2	94.5, 79.7	3.7
3^{Tr}	1.95	2.09	164.6	92.8, 80.4	42.7
4	1.96	2.07	167	92.3, 80.2	22.3
5	1.93, 1.95	2.06	174.2	94.3, 82.2	28.1
6	1.94, 1.98[a]	2.02	161	95.1, 81.2	41.8[c]
7 [28]	1.97, 2.02[a]	2.04	170.2	95.9, 81.5	33.4
8 [30]	1.97	2.06	173.4	93.2, 91	75.6
9 [26]	1.97	2.13	175.4	92.3	2.4
LPMO[11,34–37]	1.87–2.09	2.01–2.29	153–176.5	106.9–87.1	58.1–67.4

[a] Distance for Cu-Pyridine. [b] Heterocycle angle is the measured angle between planes made by the atoms of each heterocyclic ring. [c] Mean angle calculated on the disordered structures.

bound perchlorate ion bridges between adjacent copper sites (Cu–O ≈ 2.52 Å) resulting in a Cu–Cu separations of 7.26 Å and a distorted octahedral geometry around the copper. Interestingly, compound **6** appears as a monomeric copper complex. The coordinating chloride does not show any direct interaction with neighboring copper centers and is oriented towards the linker N–H of adjacent complexes, allowing for potential weak hydrogen bonding interactions (N–Cl 3.204 Å) in the solid state, though it should be noted that the N–H is disordered, with a minor part instead engaged in a hydrogen bond with a nearby perchlorate ion. This leads to a close packing of the complexes that results in substantial disruption of the square pyramidal geometry. The pyridine ring deviates from the ligand plane (angle between both heterocyclic rings is 46.6°) giving a trans N_{pyr}–Cu–N_{imid} angle of about 161° ($\tau_{4'}$ = 0.28) with a distorted square planar geometry.

The differences in packing appear to have an important effect on the angle between the two heterocyclic rings, a structural parameter recently proposed to be potentially related to the electrochemical properties and high reactivity observed in natural LPMO.[30] Consistent with their more rigid structures, resulting from the imine group, the angles between the planes of the heterocycles for complexes **1** and **2** are similar, 15.8° and 15.1° respectively. Greater variation is observed with the more flexible systems **3–5**. While in **4** and **5**, larger angles are observed (22.3° for **4** and 28.1° for **5**), in complex **3** the angle is only 3.7°. This much smaller value appears to be due to close stacking of the imidazole rings between adjacent structures in the 1-D chains. In **4** and **5**, the complexes are staggered providing more freedom for the imidazole rings. The DFT optimized structures of the monomeric forms of **3–5** (see ESI and Fig. S55†) showed angles similar for all three complexes (28.6–32.4°) and larger than the values observed in the solid state. Compound **6** displays the highest heterocycle angle of the series with a value of 46.6°. This is explained by the more distorted structure and the pyridine ring deviating from the ligand plane. The flexible nature of the linkers and imidazole units can also be seen in compound **3^{Tr}** containing the bulky trityl group. Surprisingly, this complex also forms dimers in the solid phase, with the flexibility of the structure helping to minimize steric clash between the two units by adopting more of a butterfly shape (τ_5 = 0.15).

Solution studies

The long-range axial Cu–Cl distances observed for **1–4** in the solid state and the known propensity for chlorides in *cis*-dichloro copper complexes to be exchanged for solvent in aqueous or methanolic solutions,[41,42] suggest that the dimers observed for these complexes are weakly bound. In solution, it is expected that they dissociate to give the mononuclear species. Indeed, the electron paramagnetic resonance (EPR) spectra of all complexes, recorded in frozen methanolic solution at 100 K, exhibit axial signals with $g_{\|} > g_{\perp}$, consistent with a mononuclear Cu(II) complex coordinated in a distorted square pyramidal geometry[28,30,38] (Table 2 and Fig. S9–S14†). Further, the *g*-tensor and hyperfine coupling values obtained all fall into the range of values observed for LPMO and related monomeric copper complexes,[17,38,43] suggesting similar structures and supporting that the aggregates present in the solid state for **1–4** dissociate to give the mononuclear complexes in solution. This is further supported by spin quantification experiments which showed spin/Cu ratios very close to 1 for the series of compounds at 2 mM in methanol (Fig. S15, S16 and Table S9†).

UV absorption spectra (Table 3 and Fig. S17–S29) were recorded for the complexes in aqueous solution. They all exhibit low intensity broad bands between 624 and 650 nm,

Table 2 Summary of the EPR parameters

Compound	$g_{\|\|}$	$g_{\perp}$	$\|A\|_{\|\|}$ (G)	$\|A\|_{\perp}$ (G)
1	2.265	2.061	163.3	9.8
2	2.264	2.061	161.0	11.2
3	2.261	2.060	159.7	12.9
4	2.257	2.058	163.5	11.4
5	2.266	2.064	154.7	19.8
6	2.272	2.062	163.0	7.9
LPMO[a,36]	2.226–2.28	g_x: 2.015–2.06 g_y: 2.052–2.116	116–186	$\|A\|_x$: 3–42 $\|A\|_y$: 0.5–50

[a] Performed in aqueous solutions.

Table 3 Summary of the UV visible spectrometry characteristics

Compound	Solvent	λ_{max} [nm]	ε [L mol^{-1} cm^{-1}]
1	H_2O	649	73
2	H_2O	650	73
3	H_2O	624	76
4	H_2O	633	49
4b	MeCN	611	87
4c	MeOH	627	95
5	H_2O	640	57
5b	MeCN	604	68
5c	MeOH	644	54
6	H_2O	647	79
6b	MeCN	641	129
6c	MeOH	654	132
7 [a]	H_2O	649	72
8 [30]	MeOH	662	83
9 [26]	MeOH	723	157

[a] Resynthesized.

Table 4 Summary of the electrochemical parameters

	MeOH		
Compound	$E_{1/2}$ [mV]	ΔE [mV]	Phosphate Buffer E_{red} [mV]
1	−524	139	−431
2	−518	109	−441
3	−547	147	−445
4	−542	95	−413
4[a]	−650	128	—
5	−513	100	−394
5[a]	−632	81	—
6	−464	116	−366
7[b]	−437	87	−319

[a] TBACl as support electrolyte. [b] Data recorded for the resynthesized compound.

typical of d–d transitions for copper(II) complexes in tetragonally distorted octahedral geometries, with weak axial solvent coordination[41,42] and again similar to values reported for LPMO.[24,26,28–30,36] The high intensity signals between 200 and 300 nm are assigned to $\pi \rightarrow \pi^*$ transitions of the ligands and possibly to ligand to metal charge transfer (LMCT).[44] While methylation of the imidazoles does not lead to substantial changes, the λ_{max} of the d–d transition shows a bathochromic shift of around 20 nm going from the amine to the imine complexes. A similar, though slightly smaller shift was noted for the 2-imidazole derivative complex **5** *versus* **3** and **4**. In both cases, imine or 2-imidazole, the changes are similar to what is observed when one imidazole is replaced by a pyridine unit.

Solvent effects were studied by recording the spectra of **4–6** in acetonitrile and methanol (**4b** and **4c**). While methanol leads to spectra similar to those recorded in H_2O, MeCN leads to a hypsochromic shift of the d–d transitions. This variation may be attributed to the solvent interacting with the copper at the labile positions or potentially to the presence of a monomer/dimer equilibrium in MeCN. However, concentration studies on complexes **1–6** from 2 to 0.1 mM in the different solvents all show a linear response of the absorbance suggesting limited interaction between the complexes within this concentration range.

Electrochemistry

Electrochemical analysis of the compounds, performed in MeOH with tetrabutylammonium perchlorate ($TBAClO_4$) as the electrolyte, showed a single pseudo-reversible redox event between −542 to −464 mV *vs.* ferrocene for all of the compounds (**1–6**), which is attributed to the Cu^{II}/Cu^{I} redox couple (Fig. S30–S36†). Globally, these values are lower than those observed for $CuCl_2$, reported models, and LPMO[26,28,30,36] (Table 4 and Fig. S37 and S39†). The reduction for the imine complexes is slightly higher than their amine counterparts (+23 mV and +24 mV for **1** and **2** respectively). Similarly, the 2-position connectivity of the imidazole, complex **5**, showed a 20 mV increase *vs.* **4**. When comparing **1** and **3** *versus* **2** and **4**, the methylation shows only a small influence on the redox potential with a difference between the methylated and non-methylated analogs being less than 10 mV. The introduction of a pyridine ring induced a substantial increase in the redox potential compared to the imidazole counterpart. **6** showed a 78 mV increase *versus* **4**, and the reported compound **7** showed a 76 mV gain over **5**. For this series, it appears that the electronic effects induced by changing the heterocycles are more prominent compared to other structural parameters in the first coordination sphere such as methylation or the introduction of an imine function. Within the range of dihedral angles we observed, there was no strong correlation of this structural parameter with reduction potential.

To look at the influence of the counterions associated with the complexes in solution, electrochemical studies on compounds **4** and **5** were additionally performed with TBACl instead of $TBAClO_4$. Switching between non-coordinating ions, present in **5**, for the coordinating chloride ions, present in **4**, would be expected to have a larger effect on the redox potentials of **5**. However, the change for the two compounds is similar. The reduction potentials decrease by 108 for **4** and 119 mV for **5**. This implies that in MeOH solutions with non-coordinating counterions, the chlorides are largely replaced by solvent molecules or the ions from the electrolyte, and supports the other solutions studies which suggest that the dimers observed in the solid state are dissociated in solution.

Reactivity assays

The oxidative reactivity of the complexes **1–7** was tested using the *p*-nitrophenyl-β-D-glycopyranoside (PNPG) assay, Scheme 2.[28] These tests were conducted in a phosphate buffer (pH = 7.5) using 10 mM PNPG with 4 equivalents of H_2O_2 as the oxidant and a catalytic loading of 0.5 mol%.[29] The PNPG degradation was monitored by tracking the releases of the *para*-nitrophenolate (PNP). Under the conditions used, it is reported that roughly 75% of the *para*-nitrophenol is deprotonated giving the characteristic absorption at 400 nm.[29]

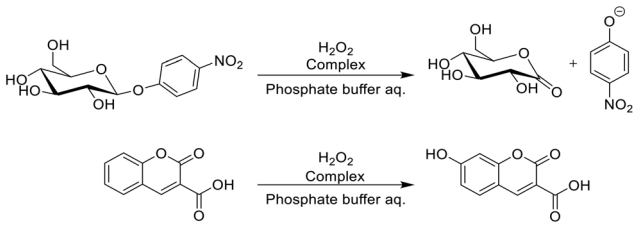

Scheme 2 (Top) Oxidative cleavage of *p*-nitrophenyl-β-D-glycopyranoside (PNPG). (Bottom) Coumarin-3-carboxylic acid (CCA) hydroxylation.

All complexes tested in this paper show sigmoidal curves for product formation under the described conditions (Fig. 3 top, S41 and S42†). An induction period is observed during which no significant product is formed, followed by sudden substrate degradation. The induction period varies from 3 minutes for complex **7** to 92 minutes for compound **1**, and differs only a few minutes for each compound when the tests are repeated.

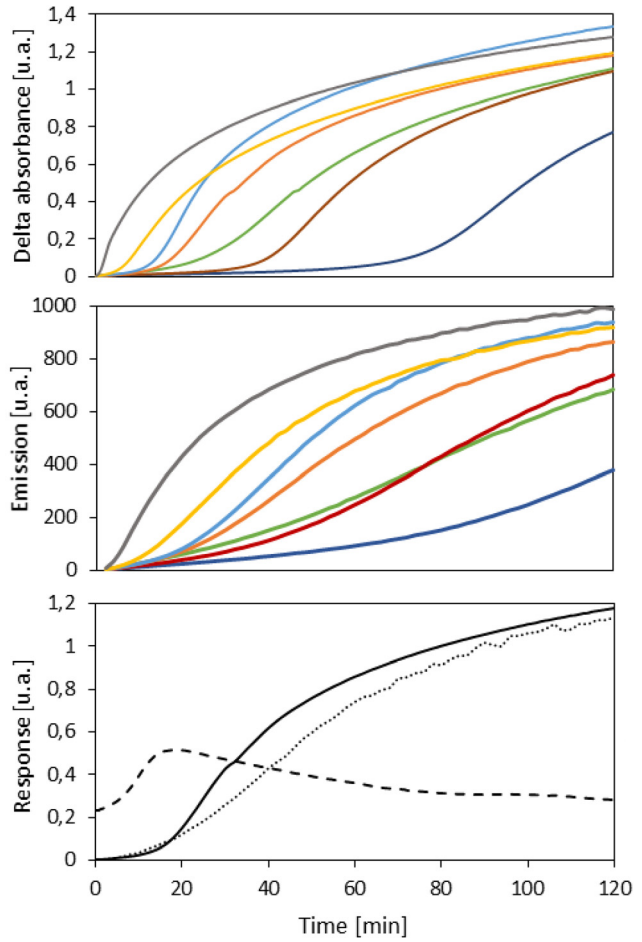

Fig. 3 (Top) Evolution over time of *p*-nitrophenolate absorbance (at 400 nm) produced from the degradation of PNPG by the compounds **1** (dark blue), **2** (green), **3** (red), **4** (orange), **5** (light blue), **6** (yellow) and **7** (grey). (Center) Evolution over time of 7-hydroxycoumarin-3-carboxylic acid fluorescence (at 447 nm) produced from the hydroxy radical trap coumarin-3-carboxylic acid with compound **1–7** (same colors as for Top). (Bottom) Comparison between the evolution over time of (dash line) the absorbance (at 305 nm) of the intermediate species after addition of 800 equivalents of H_2O_2, (plain line) *p*-nitrophenolate absorbance (at 400 nm) and (dots line) 7-hydroxycoumarin-3-carboxylic acid fluorescence (at 447 nm) for compound **4**.

The time for the upsurge and the maximum production rate were obtained by taking the derivative of the evolution of the absorbance over time for each compound and data are presented in Table 5 (Fig. S44†). Complex **4**, because of its moderate induction period, was used to study the effects of catalyst and H_2O_2 concentration. Doubling the concentration of catalyst decreases the induction period by about half (12.5 minutes), while doubling the H_2O_2 concentration has a larger effect, decreasing by ~3/4 the time required to obtain the maximum rate (6.5 minutes) (Fig. S45†). Incubating the complex with the substrate, for 10 minutes or 1 hour, prior to H_2O_2 addition, did not lead to differences in the observed reactivity. However, adding H_2O_2 20 or 60 minutes prior to PNPG substrate addition effectively removes the induction period, though waiting 60 minutes results in a substantial decrease in activity (Fig. S46†).

After 24 h, the yield of the reaction with all complexes reaches around 2.2% which is comparable to other LPMO active site models tested on the same substrate. Most compounds produced roughly the same amount of chromophore after the reaction, which may be due to degradation of the complexes from auto-oxidation of the ligand. Indeed, after the initial upsurge, the slope of the product formation *versus* time becomes similar to that of the free copper salt. Adding another equivalent of catalyst or H_2O_2 to the catalytic assay after 1 hour leads to only a slight increase in nitrophenolate production, but rates observed after the initial induction period are not reobtained (Fig. S47†). After 2 h adding more H_2O_2 does not lead to any appreciable increase in rate, suggesting almost complete inactivation of the complexes.

Relative to the structural modifications, it appears that the presence of an imine greatly increases this induction period *versus* the corresponding amine complexes, (40 min and 92 min *vs.* 24 min and 49 min). Surprisingly, while the presence of the methyl on the imidazole had little effect on the spectroscopic or electrochemical properties of the complexes, it leads to a substantial decrease in the activation period compared to the non-methylated derivative (24 min for **4** *vs.*

Table 5 Summary of the catalytic assays

Compound	Time of V_{max} [min]	V_{max} [μM min^{-1}]	Yield[b] [%]	TON[b]
1	92	1.341	2.27	4.55
2	40	1.456	2.26	4.52
3	49	1.744	2.27	4.54
4	24	2.155	2.21	4.42
5	19	3.121	2.4	4.79
6	10	2.292	2.24	4.47
7[a]	3	5.441	2.21	4.42
$CuCl_2$	—	—	2.16	4.13

[a] Resynthesized complex. [b] Calculated after 24 h.

49 min for **3** and 40 min for **2** *vs.* 92 min for **1**). It was also observed that the presence of the pyridine moiety greatly reduces the activation period as shown by the comparison of **6** with **3** and **4** (10 min *vs.* 49 min and 24 min respectively) as well as between **7** and **5** (3 min *vs.* 19 min). The use of a 2-position linked imidazole also appears to slightly reduce the lag time as seen in comparing **4** (24 min) and **5** (19 min). However, these values are close and minor experimental variation may account for this difference. Still, on average across multiple runs, the lag time for **5** was shorter than for **4**, Fig. S43.† The same trend is observed for the maximum reaction speed: the use of a pyridine or a 2-position imidazole gives a greater maximum conversion rate than the 4-position imidazole. The presence of an amine function in place of an imine and the *N*-methylation of the imidazole both slightly increase the rate. These observations together are coherent with **7** having the shortest lag time and the highest conversion rate.

It should be noted that the counter-ion (ClO_4^- *vs.* Cl^-) has a low impact on the catalytic assay, the perchlorate containing compound **5** in presence of 1 or 10 equivalents of chloride did not lead to any significant variations, further supporting the limited association of the counterions as seen in the electrochemical studies. Globally, for the amine linker complexes, the lag time is inversely correlated with the reduction potentials of the compounds recorded in MeOH, *i.e.* the more easily reduced compounds display the fastest onset times. When CVs were recorded in the buffer solution used for the catalytic assays (Fig. S39 and Table S10†) the correlation was better, with the ease of reduction for compounds **2–7** matching the order of their induction periods (Fig. S40†). Notably, a larger difference was observed between **3** and **4**. This may be due to differences in the interaction of the methylated and non-methylated imidazoles with the medium or differences in protonation equilibria, and can explain the differences in the observed lag times. Unfortunately, the anomalous behavior of compound **1** in the buffer solution made further comparison of the effect of methylation (*i.e.* between **1** and **2**) difficult.

It has been discussed in the literature that the produced *para*-nitrophenolate can undergo further degradation leading to an underestimation of product formation.[29] The degradation of PNP by the complexes was assayed using the same conditions as for the PNPG reactivity, Fig. S48.† Over a 2-hour period, the degradation reached 75–92% across the series of complexes, revealing an important competition between the *para*-nitrophenolate production and its degradation suggesting a significant underestimation of the oxidative properties of the compounds. The relative reactivity of the compounds mostly aligns with PNPG degradation, however a few differences where noted. Complex **4** degrades PNP faster than **5** while the opposite trend is observed for the PNPG assay. The radical trap experiment shows a close reactivity, it is thus proposed that complex **4** and **5** produce an almost similar amount hydroxy radicals but as **4** degrades PNP faster the apparent PNPG degradation is lowered. Complex **2** on the other hand displays a lower reactivity towards PNP degradation, being similar to complex **1**. This may be due to differences in the mechanism for PNP degradation *versus* PNPG, but suggests that the presence of the imine may limit the reactivity of the complexes.

To look further into the reactivity, the four best performing compounds, complexes **4–7**, were mixed with hydrogen peroxide in the absence of PNPG and the UV-visible spectra were recorded. A new species with an absorption band at 305 nm was observed, which then decays over approximately 15 minutes (Fig. S49†). The species still displays the typical d–d transition around 650 nm consistent with a Cu(II) complex, and based on previous reports,[28] the band at 305 nm is assigned to a LMCT transition of a Cu(II)OOH intermediate. This intermediate forms during the induction times observed for the compounds, though builds up slightly faster for **5** than for **6**, opposite to their respective induction periods (Fig. S50†). However, the intensity of the absorption band as well as its decay in the absence of PNPG correlate well with the maximum speeds recorded in the catalytic assays, *i.e.* **5** and **7** have faster maximum rates, while **6** and **4** are similar.

The formation and decay of the intermediate also coincide with production of hydroxyl radicals. Coumarin-3-carboxylic acid was used as a hydroxyl radical trap under the conditions of the catalytic assays but without PNPG. The formation of 7-hydroxycoumarin-carboxylic acid was followed by fluorescence spectroscopy, monitoring the emission at 447 nm, hydroxyl radical production is evidenced with all of the complexes (Fig. 3 center and Fig. S51†). Moreover, like for the assays with PNPG, sigmoidal kinetics are also observed for the production of hydroxyl radicals, with the induction periods being similar to what is observed for the onset of p-nitrophenolate production and correlated with the decay of the proposed Cu(II)OOH species, Fig. 3 bottom. This suggests that hydroxyl radicals produced by the complexes are the main agent responsible for the degradation of PNPG. Competition studies with PNPG and coumarin-3-carboxylic acid further support this free radical mechanism (Fig. S52†). In the presence of the coumarin (PNPG : coumarin = 4 : 1), the formation of *para*-nitrophenolate over 2 hours is decreased by more than 50%. Of note, $CuCl_2$ showed a higher hydroxyl radical production than all the complexes, with the exception of **7**, yet it showed poor PNPG degradation. This is likely due to the formation of the reported copper coumarin-3-carboxylate complex in aqueous solution.[45] The resulting complex is likely at the origin of the more important hydroxyl radical production observed in the coumarin-3-carboxylic acid assay.

The production of hydroxyl radicals from copper complexes or salts is well known in the literature and different mechanisms have been proposed involving different Cu oxidation states for their formation and reaction with substrates, Scheme 3. With only Cu(II), (Cu(II) mechanism), direct homolytic OO bond cleavage of a Cu(II)–OOH species can occur to give a Cu(II)–O$^\bullet$ and HO$^\bullet$, followed by H atom abstraction from the substrate, R–H, to give R$^\bullet$.[22,46] In the simplest metal centered termination, recombination with Cu(II)–O$^\bullet$ and protonation provides the hydroxylated product and the starting Cu(II). Alternatively, (Cu(I) mechanism) reduction of Cu(II) to Cu(I),

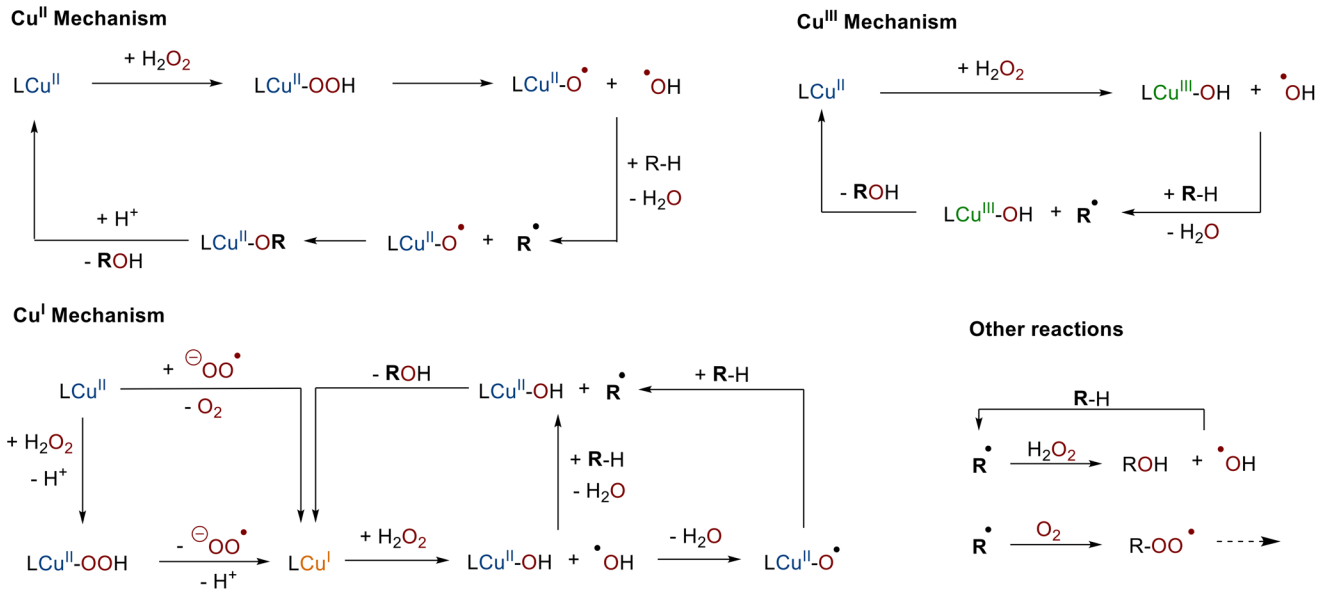

Scheme 3 Mechanisms for hydroxyl radical production and substrate (R–H) activation that have been proposed for copper complexes.[45–47]

either by homolytic Cu–O bond cleavage or by another species in solution can allow for Fenton-like chemistry,[46] where Cu(I) reacts with H_2O_2 to give Cu(II)–OH and HO•. The hydroxy radical can do the H-atom abstraction followed by rebound with the Cu(II)–OH to give the oxidized product and a Cu(I), or the HO• abstracts an H-atom from Cu(II)–OH to give Cu(II)–O• which then does the abstraction from the substrate. The latter is proposed as a mechanism for LPMOs when hydrogen peroxide is the oxygen cosubstrate.[47] Additionally, a Cu(III) mechanism has been described involving similar Fenton-like steps as for the Cu(I) mechanism.[48,49]

For the model complexes described in this work, the Cu(II)/Cu(III) mechanism is excluded based on the electrochemical results. Additionally, the simplest Cu(II) mechanism involving recombination and reforming of the starting Cu(II) complex would not explain the induction periods observed, as the initial slow step would occur in each cycle. Rather, the induction period suggests that there is either a slow activation of the complexes to give the catalytically active species or that once the reaction begins, one of the products or intermediates can activate the complex or otherwise propagate a chain reaction.[50] For the Cu(II) mechanism, this could still involve the initial production of the hydroxyl radicals and H-atom abstraction, with the substrate radical going on to react with O_2 to give an organic peroxy radical capable of another H-atom abstraction, or, for PNPG, the substrate radical could react with H_2O_2 to generate another equivalent of HO•. Still, while such chain reaction descriptions could be suitable for PNPG, where H-atom abstraction is the crucial mechanistic step, the possibility of propagation of the reaction of hydroxyl radicals with coumarin-3-carboxylic acid is less clear.[51] Based on this, the activation of the complexes to give a more reactive species is the most likely possibility and would be consistent with the observed build-up and decomposition of the intermediate species preceding HO• production. The nature of the active structure, and whether it is a Cu(II) or Cu(I) complex, remains to be determined. However, as the induction periods correlate with the ease of reduction of the complexes, it is possible that the decay of the intermediate may involve the formation of a Cu(I) complex and a subsequent Fenton-like mechanism. The reduction could come from either homolytic cleavage of the Cu–O bond in a Cu–OOH intermediate or by one of the radical species generated by either an initial Cu(II) mechanism or a Fenton-like mechanism with residual copper salts in solution. Indeed, nanomolar concentrations of Cu(II) salts have been shown to promote Fenton-like chemistry, with the Cu(II) ion being reduced by H_2O_2,[52,53] and the presence of this amount of free Cu(II) cannot be ruled out. To look at the possibility of reduction of the Cu(II) complexes, ascorbic acid was added to the assays with the coumarin-3-carboxylic acid (Fig. S53 and S54†). The results are complicated to interpret as ascorbate alone can reduce H_2O_2, leading to formation of 7-hydroxycoumarin-3-carboxylic acid over ten minutes. However, in the presence of the complexes and ascorbate, the addition of H_2O_2 leads to nearly an equal amount of 7-hydroxycoumarin-3-carboxylic acid in the time required for mixing the sample (<1 minute). While the presence of ascorbate is less relevant to the reducing species that would be present in the PNPG or coumarin-3-carboxylic acid reactions, this nevertheless suggests that the reduction to a Cu(I) species may indeed be important for the reactivity observed for the complexes.

Conclusions

The importance of the histidine brace for copper biochemistry can be seen in its prevalence in different enzymes. In addition

to LPMO, it has also been observed in particulate methane monooxygenase,[54] copper-binding protein CopC,[55] spindles of the fusolin protein produced by entomopoxviruses,[56] and fungal protein Bim 1,[57] highlighting a range of roles for this coordination motif. In this work, we have described the synthesis and characterization of a series of copper imidazole complexes based on N_3 ligands related to the histidine brace, which display variation in the methylation of the imidazole rings, the 2-/4-connectivity of the imidazole, the amine/imine nature of the linker, and presence of a pyridine *vs.* imidazole. The compounds show similar T-shaped N_3 coordination as in LPMOs and display similar EPR and UV-vis spectroscopic properties. Still, the structural variations have moderate effects on the electrochemical properties, especially in the buffer solution used for the reactivity studies. This appears to be largely based on the electronic nature of the modifications, for example with complex **6**, the presence of a pyridine moiety overshadows the other changes leading to the largest positive shifts for the Cu(II)/Cu(I) reduction. Meanwhile, methylation of the imidazoles results in slight increase in the reduction potential *versus* the non-methylated complexes in MeOH, but has a much larger effect in the phosphate buffer solution. Similarly, both the 2-connected imidazoles and imines also displayed more positive reductions than the amine linker 4-connected imidazole derivatives, **3** and **4**. This is particularly interesting in the case of the connectivity of the imidazoles as it suggests important differences in the donor/acceptor strengths of these units.

The oxidative reactivity of the compounds was tested with the PNPG assay and also showed structure dependent behavior. Unlike previous LPMO models, all of the complexes described in this work show sigmoidal kinetics for the degradation of the substrate, with lag times for the compounds ranging between 3–90 minutes prior to product formation. Importantly, the lag times allowed to relate the PNPG reactivity with both the formation and decay of an intermediate resulting from reaction of H_2O_2 with the complexes and the time observed for hydroxyl radical production using coumarin-3-carboxylic acid as a hydroxyl radical trap. These steps correlate well with the observed reduction potential trend for the compounds in the same buffer. The more easily reduced or less electron rich the compound, the shorter the lag time. This can be expected to influence both the binding of peroxide and homolytic cleavage steps required for hydroxyl radical production. Thus, the differences in reactivity appear to be primarily due to the electronic differences imparted by the structural modifications. This gives interesting implications for the design of LPMO inspired catalysts and supports a free radical mechanism being the main pathway for the PNPG degradation in the case of these complexes.

Experimental

Chemicals and synthesis

All commercial reagents and solvents were obtained from Sigma-Aldrich, Acros Organics or Fluorochem, and were used as purchased without further purification unless otherwise stated. Dry solvents were obtained by standard procedures according to D. D. Perrin and D. R. Perrin, Purification of Laboratory Chemicals. Tetrahydrofuran and diethylether were purified by distillation from benzophenone ketyl radical. Dichloromethane, toluene, trimethylamine and trimethylsilyl chloride were purified by distillation from calcium hydride. Technical grade ethyl acetate and petroleum ether (40 to 65 °C fraction) were distilled under reduced pressure. Analytical thin layer chromatography (TLC) was carried out on Merck Millipore F254 silica gel 60 plates (210–270 μm thickness, aluminium supported). The plates were visualized using ultraviolet light (254 nm). Flash column chromatography was carried out on ROCC silica gel 60 Å (230–400 Mesh). *N*-Methylhistamine and 1-trityl-Imidazole-4-carboxaldehyde were synthesized through modified reported procedures described in the ESI.† The detailed procedures and characterizations of ligands **3–7** and complexes **1–7** are further described in the ESI.† **Caution!** Copper perchlorate is category 2 oxidizing solid and potentially explosive. All due precautions should be taken.

Synthesis of L3

The suspension of L3Tr (1 g, 2.31 mmol, 1 eq.) in aqueous HCl (40 mL, 1 M) was stirred at room temperature overnight. The resulting suspension was filtered and the filtrate was evaporated under vacuum to afford **L3** as a white powder (0.566 g, 93%) ^{1}H NMR (300 MHz, d6-DMSO) δ (ppm): 9.16 (d, J = 1.2 Hz, 1H), 9.07 (d, J = 1.3 Hz, 1H), 7.88 (s, 1H), 7.58 (s, 1H), 4.34 (s, 2H), 3.35–3.28 (m, 2H), 3.22–3.14 (m, 3H). ^{13}C NMR (75 MHz, d6-DMSO) δ (ppm): 134.90, 134.41, 128.99, 124.54, 121.01, 117.39, 44.72, 21.36.

Synthesis of L4

The suspension of L4Tr (0.75 g, 1.67 mmol, 1 eq.) in aqueous HCl (40 mL, 1 M) was stirred at room temperature overnight. The resulting suspension was filtered and the filtrate was evaporated under vacuum to afford the product as a white powder (0.401 g, 86%). ^{1}H NMR (300 MHz, d6-DMSO) δ (ppm): 9.14 (d, J = 1.2 Hz, 1H), 9.05 (d, J = 0.7 Hz, 1H), 7.88 (d, J = 1.0 Hz, 1H), 7.60 (d, J = 1.0 Hz, 1H), 4.33 (s, 2H), 3.82 (s, 3H), 3.29 (t, J = 7.3 Hz, 2H), 3.20–3.14 (t, J = 7.3 Hz, 2H). ^{13}C NMR (75 MHz, d6-DMSO) δ (ppm): 136.00, 134.95, 129.34, 124.53, 121.51, 121.06, 44.80, 35.96, 21.39.

Synthesis of L5

To a solution of 1*H*-imidazole-2-carbaldehyde (1 g, 10.19 mmol, 1 eq.) and a3 (2.02 g, 10.19 mmol, 1 eq.) in dry methanol (50 mL, dried on 3 Å molecular sieves) under argon were added 3 Å activated molecular sieves and sodium hydroxide (0.774 g, 19.36 mmol, 1.9 eq.). The solution was stirred 2 h at room temperature and $NaBH_4$ (0.771 g, 20.39 mmol, 2 eq.) was added. After 3 h at room temperature the mixture was filtered and evaporated under vacuum. The resulting solid was suspended in water (100 mL) and extracted with dichloromethane (3 × 75 mL) and followed with a solution of isopropanol (25%) in chloroform (3 × 100 mL). The isopropanol

phases were gathered, dried on Na_2SO_4 and evaporated under vacuum to afford the product **L5** as a white solid (1.129 g, 55%). ^{1}H NMR (300 MHz, d6-DMSO) δ (ppm): 7.42 (d, J = 0.7 Hz, 1H), 6.87 (s, 1H), 6.80 (s, 1H), 3.69 (s, 2H), 3.57 (s, 3H), 2.70 (t, J = 6.9 Hz, 2H), 2.55 (t, J = 7.1 Hz, 2H). ^{13}C NMR (75 MHz, d6-DMSO) δ (ppm): 147.59, 140.47, 137.54, 117.19, 49.48, 46.95, 33.12, 28.81. HRMS (ESI): m/z calculated for $C_{10}H_{16}N_5$ $[M + H]^+$ 206.14002, found 2016.13987.

Synthesis of L6Tr

To a solution of a4 (0.554 g, 1.637 mmol, 1 eq.) and 2-pyridylethylamine (0.2 g, 1.637 mmol, 1 eq.) in dry methanol (25 mL, dried on 3 Å molecular sieves) under argon were added 3 Å activated molecular sieves and sodium acetate (0.134 g, 1.637 mmol, 1 eq.). The solution was stirred 4 h at room temperature and $NaBH_4$ (0.124 g, 3.274 mmol, 2 eq.) was added. After 2 h at room temperature the mixture was filtered and evaporated under vacuum. The resulting solid was suspended in water (75 mL) and extracted with dichloromethane (3 × 75 mL), the organic phases were gathered, dried on Na_2SO_4 and evaporated under vacuum. The crude product was purified over flash silica gel chromatography (methanol–NH_3 (7N)/DCM, 3 : 97) to afford the product L6Tr as a white solid (0.314 g, 43%). ^{1}H NMR (300 MHz, d6-DMSO) δ (ppm): 8.42 (ddd, J = 4.9, 1.8, 0.9 Hz, 1H), 7.64 (td, J = 7.6, 1.9 Hz, 1H), 7.45–7.35 (m, 9H), 7.27 (d, J = 1.4 Hz, 1H), 7.17 (ddd, J = 8.4, 6.0, 4.5 Hz, 2H), 7.12–7.04 (m, 6H), 6.69 (d, J = 1.1 Hz, 1H), 3.56 (s, 2H), 2.82 (s, 4H). ^{13}C NMR (75 MHz, d6-DMSO) δ (ppm): 160.78, 149.39, 142.86, 140.65, 138.19, 136.80, 129.72, 128.72, 128.49, 123.55, 121.73, 118.85, 74.92, 49.06, 47.18, 38.28. HRMS (ESI): m/z calculated for $C_{30}H_{29}N_4$ $[M + H]^+$ 445.2392, found 445.2394.

Synthesis of L6

The suspension of L6Tr (0.314 g, 0.706 mmol, 1 eq.) in aqueous HCl (15 mL, 1 M) was stirred at room temperature overnight. The resulting suspension was filtered and the filtrate was evaporated under vacuum to afford the product **L6** as a white powder (0.194 g, quantitative). ^{1}H NMR (300 MHz, d6-DMSO) δ (ppm): 10.27 (s, 2H), 9.16 (d, J = 1.3 Hz, 1H), 8.76 (dd, J = 5.5, 0.9 Hz, 1H), 8.35 (td, J = 7.8, 1.3 Hz, 1H), 7.95–7.84 (m, 2H), 7.79 (d, J = 6.5 Hz, 1H), 4.36 (s, 2H), 3.53–3.41 (m, 4H). ^{13}C NMR (75 MHz, d6-DMSO) δ (ppm): 152.92, 145.64, 143.12, 134.98, 127.79, 125.74, 124.54, 121.05, 44.91, 39.57, 31.24. HRMS (ESI): m/z calculated for $C_{11}H_{15}N_4$ $[M + H]^+$ 203.1297, found 203.1296

Synthesis of L7

To a solution of 1-methyl-2-imidazolecarboxaldehyde (0.1 g, 0.908 mmol, 1 eq.) and 2-pyridylethylamine (0.111 g, 0.108 mL, 0.908 mmol, 1 eq.) in dry methanol (10 mL, dried on 3 Å molecular sieves) under argon were added 3 Å activated molecular sieves and sodium acetate (0.075 g, 0.908 mmol, 1 eq.). The solution was stirred 3 h at room temperature and $NaBH_4$ (0.069 g, 1.816 mmol, 2 eq.) was added. After 2 h at room temperature the mixture was filtered and evaporated under vacuum. The resulting solid was suspended in a saturated bicarbonate aqueous solution (50 mL) and extracted with dichloromethane (3 × 50 mL). The organic phases were gathered, dried on Na_2SO_4 and evaporated under vacuum. The crude was purified over flash silica gel chromatography (methanol/NEt_3/DCM, 5 : 1 : 94) to afford the product **L7** as a white solid (0.097 g, 50%). ^{1}H NMR (300 MHz, $CDCl_3$) δ (ppm): 8.55–8.48 (m, 1H), 7.58 (td, J = 7.7, 1.8 Hz, 1H), 7.19–7.06 (m, 2H), 6.90 (d, J = 1.1 Hz, 1H), 6.79 (d, J = 1.0 Hz, 1H), 3.87 (s, 2H), 3.61 (s, 3H), 3.10–3.01 (m, 2H), 3.02–2.92 (m, 2H).

Synthesis of 1

1*H*-Imidazole-4-carbaldehyde (0.097 g, 1.1 mmol, 1 eq.), histamine dihydrochloride (0.186 g, 1.1 mmol, 1 eq.) and copper perchlorate hexahydrate (0.374 g, 1.1 mmol, 1 eq.) were dissolved in MeOH (6 mL). The mixture was stirred at room temperature overnight. The resulting suspension was cooled down to 0 °C and filtered. The solid was collected, triturated in diethyl ether, filtered and dried under vacuum to afford the complex 1 as a blue powder (0.141 g, 33%). HRMS (ESI) m/z calculated for $C_9H_{11}ClCuN_5$ $[M + Cl^-]^+$ 286.99990, found 286.99924. Elemental analysis: calculated for $C_9H_{11}N_5Cl_2CuO_4$, C, 27.88; H, 2.86; N, 18.07. Found C, 27.96; H, 2.84; N, 18.02.

Synthesis of 2

1*H*-Imidazole-4-carbaldehyde (0.097 g, 1.1 mmol, 1 eq.), a3 (0.2 g, 1.1 mmol, 1 eq.) and copper perchlorate hexahydrate (0.374 g, 1.1 mmol, 1 eq.) were dissolved in MeOH (6 mL). The mixture was stirred at room temperature overnight. The resulting suspension was cooled down to 0 °C and filtered. The solid was collected, triturated in diethyl ether, filtered and dried under vacuum to afford the complex **2** as a blue powder (0.159 g, 36%). HRMS (ESI) m/z calculated for $C_{10}H_{13}ClCuN_5$ $[M + Cl]^+$ 301.01555, found 301.01495, m/z calculated for $C_{11}H_{14}CuN_5O_2$ $[M + Formiate]^+$ 311.04435, found 311.04378. Elemental analysis: calculated for $C_{10}H_{13}N_5Cl_2CuO_4$, C, 29.9; H, 3.26; N, 17.44. Found C, 29.9; H, 3.25; N, 17.17.

Synthesis of 3

L1 (0.136 g, 0.711 mmol, 1 eq.) and copper perchlorate hexahydrate (0.263 g, 0.711 mmol, 1 eq.) were dissolved in MeOH (4 mL). The mixture was stirred overnight at room temperature, diethylether was then added to the crude and a blue powder was filtered. Slow diffusion of ether in a methanol solution of the complex yielded the pure compound **3** (0.55 g, 20%). HRMS (ESI): m/z calculated for $C_9H_{13}N_5ClCu[M + Cl]^+$ 289.01555, found 289.01485. Elemental analysis: calculated for $C_9H_{13}N_5Cl_2CuO_4{\cdot}H_2O$, C, 26.51; H, 3.71; N, 17.18. Found C, 26.33; H, 3.36; N, 16.38.

Synthesis of 3^{Tr}

L3Tr (0.1 g, 0.231 mmol, 1 eq.) and copper chloride anhydrous (0.031 g, 0.231 mmol, 1 eq.) were dissolved in 3 mL of a acetonitrile/MeOH mixture (5 : 1 v/v). The mixture was stirred at room temperature, after 5 minutes KPF_6 (0.085 g, 0.462 mmol,

2 eq.) was added and the resulting suspension was stirred at room temperature for 5 minutes. The precipitate was filtered and ether (100 mL) was added to the filtrate. The resulting suspension was filtered and washed with ether to yield the complex $\mathbf{3^{Tr}}$ as a blue powder (0.154 g, 98%). HRMS (ESI): *m*/*z* calculated for $C_{28}H_{27}N_5CuCl$ $[M + Cl]^+$ 531.12455, found 531.12472.

Synthesis of 4

L4 (0.2 g, 0.447 mmol, 1 eq.) and copper perchlorate hexahydrate (0.16 g, 0.447 mmol, 1 eq.) were dissolved in MeOH (2 mL). The mixture was stirred at room temperature, after 2 h triethylamine (0.09 g, 0.894 mmol, 2 eq.) was added and the suspension filtered. The solid was resuspended in methanol and trifluoracetic acid was added (0.102 g, 0.894 mmol, 2 eq.), the resulting solution was stirred 2 h at room temperature then evaporated under vacuum. Slow diffusion of ether in a methanol solution of the complex yielded the pure compound **4** (0.255 g, 37%). HRMS (ESI): *m*/*z* calculated for $C_{10}H_{15}N_5CuCl$ $[M + Cl]^+$ 303.03120, found 303.03073. Elemental analysis: calculated for $C_{10}H_{15}N_5Cl_2CuO_4$, C, 29.75; H, 3.75; N, 17.35. Found C, 29.86; H, 3.72; N, 17.05.

Synthesis of 5

L5 (0.1 g, 0.487 mmol, 1 eq.) and copper perchlorate hexahydrate (0.181 g, 0.487 mmol, 1 eq.) were dissolved in MeOH (2 mL). The mixture was stirred 4 h at 60 °C then room temperature overnight. Diethylether was then added to the crude and the solution was filtered to afford the complex **5** as a blue crystalline powder (0.120 g, 48%). HRMS (ESI): *m*/*z* calculated for $C_{10}H_{15}N_5Cu$ $[M - H^-]^+$ 267.05397, found 267.05389. Elemental analysis: calculated for $C_{10}H_{15}N_5Cl_2CuO_8{\cdot}2H_2O$, C, 23.83; H, 3.80; N, 13.90. Found C, 23.43; H, 3.84; N, 13.34.

Synthesis of 6

L6 (0.2 g, 0.727 mmol, 1 eq.) and copper perchlorate hexahydrate (0.269 g, 0.727 mmol, 1 eq.) were dissolved in MeOH (10 mL). The mixture was stirred overnight at room temperature, diethylether was then added to the crude and a blue powder was filtered. Slow diffusion of ether in a methanol solution of the complex yielded the pure compound **6** (0.0845 g, 28%). HRMS (ESI): *m*/*z* calculated for $C_{11}H_{14}N_4Cu$ $[M - H^-]^+$ 300.02030, found 300.01959. Elemental analysis: calculated for $C_{11}H_{14}N_4Cl_2CuO_4$, C, 32.97; H, 3.52; N, 13.98. Found C 32.34; H 3.33; N, 13.81.

Synthesis of 7

L7 (0.0972 g, 0.449 mmol, 1 eq.) and copper perchlorate hexahydrate (0.166 g, 0.449 mmol, 1 eq.) were dissolved in MeOH (3 mL). The mixture was stirred overnight at room temperature, diethylether was then added to the crude and a blue powder was filtered. Slow diffusion of ether in a methanol solution of the complex yielded the pure compound **7** (0.162 g, 71%). Elemental analysis: calculated for $C_{13}H_{20}N_4Cl_2CuO_9$, C, 30.57; H, 3.95; N, 10.97. Found C, 30.31; H, 3.87; N, 10.75.

Nuclear magnetic resonance

Proton nuclear magnetic resonance (^{1}H NMR) spectra were recorded using Bruker Avance II-300 (300 MHz) spectrometers. Carbon nuclear magnetic resonance (^{13}C NMR) spectra were recorded using Bruker Avance II-300 (75 MHz) spectrometers. Chemical shifts (δ) are reported in parts per million (ppm) relative to residual solvent peaks: 1H ($CDCl_3$ δppm = 7.26, d6-DMSO δ ppm = 2.50, D_2O δ ppm = 4.79), 13C (d6-DMSO δ ppm = 39.5). Coupling constants are reported in Hertz (Hz). Splitting patterns are designed as: s (singlet), d (doublet), t (triplet), q (quartet), and m (multiplet).

High resolution mass spectroscopy

Mass spectra were recorded by the Mass Spectrometry Service of the "ASM" platform from the Institute of Condensed Matter and Nanosciences (IMCN) at UCLouvain, using Q-Tof Waters Synapt XS spectrometers with a Thermo Orbitrap Exactive device. The values are given in Dalton.

X-Ray diffraction crystallography

All diffraction data were recorded on a MAR345 image plate using Mo-Kα radiation generated by an Incoatec IμS microfocus source (Montel Mirrors). All crystals were stable and measured at ambient conditions. Data integration and reduction was carried out using the CrysAlisPRO software package, and the implemented absorption correction was applied. The structures were solved by dual space direct methods (SHELXT) and refined against F2 by SHELXL-2018/3 or 2019/3. All non-hydrogen bonds were refined anisotropically, hydrogen atoms were added in calculated positions and refined in riding mode, with temperature factors 1.2 times higher than their parent atoms (1.5 for methyl hydrogens).

In 1 the perchlorate anion was slightly disordered over two positions (65/35 ratio) with isotropic restraints added for the minor part. Similar disorder is observed for the perchlorate anion in 2 (about 50/50 ratio). 3 crystallizes is a non-centrosymmetric space group and was refined as an inversion twin and overall isotropic and rigid bond restraints were applied to the ligand. In 4 the perchlorate anion is also disordered (80/20 ratio) and isotropic and rigid bond restraints were applied to the minor part. In 5 both perchloride anions are found disordered (each 67/33 ratio) and geometric restraints as well as isotropic and rigid bond restraints were applied. For the non-coordinating perchlorate thermal ellipsoids of the minor part were constraint to be equal to the major part. In 6 the ligand is found disordered over two sites (82/18 ratio). Overall the disordered parts appear to be superposed onto each other with minimal deviation from each other, apart from the inverted chirality on the linker N-atom (centrosymmetric space group). The central NH is engaged in a hydrogen bond with a neighbouring Cl (major part); or forms a H-bond to the oxygen of the disordered perchlorate anion (57/43 ratio) for the minor part. The minor part of the ligand is restraint to be geometrically similar to the major part. Isotropic and rigid bond

restraints were set up for the disordered ligand and perchlorate anion.

Electron paramagnetic resonance

CW-EPR spectra were recorded at 100 K (frozen solutions), on a Bruker Magnettech ESR5000 EPR spectrometer operating at ~9.5 GHz (X-band). Unless otherwise stated, 10^{-3} M solutions of copper complexes were prepared in methanol. Samples were contained in 3 mm OD quartz tubes closed with PE caps. The EPR spectra were obtained with the following spectrometer settings: microwave power: 20 mW; modulation amplitude: 0.7 mT and modulation frequency: 100 kHz. The number of scans was 4. Data handling was performed on the Bruker ESR Studio version 1.90.0 software. All spectra are shown after baseline correction. The Spin Count software module (Bruker) was used for quantitative measurements. Results of the quantification were confirmed using a copper disodium ethylenediaminetetraacetate solution ($Cu(II)EDTA(Na)_2$) and acquisition of a spectrum in the same conditions before and after the spectra of the samples. The simulations of CW EPR spectra were run with Easyspin 6.0.6[58] using the 'pepper' function with one electron spin $S = \frac{1}{2}$ (Cu unpaired electron). All parameters were optimized using 'esfit' function.

UV/Visible spectroscopy

The spectra were recorded on a VWR UV-1600PC Scanning Spectrophotometer equipped with Deuterium/Tungsten Halogen Lamp.

Electrochemistry

The experiments were carried out in a 10 mL three electrode glass cell with a glassy carbon working electrode (d = 3 mm), a platinum wire counter electrode, and a Ag^+/Ag pseudo reference electrode. Unless otherwise stated, voltammograms were recorded in methanol with 0.1 M tetrabutylammonium perchlorate under an argon atmosphere, at room temperature and at a scan rate of 100 mV s^{-1}. Ferrocene was used as an internal standard.

Elemental Analysis (CHNS) was done with ThermoTM FlashSmartTM Elemental Analyzer.

Reactivity assays

A 1 mL UV quartz cuvette was charged using micropipettes, with 500 μL of catalyst solution (0.1 mM in buffer), 100 μL of the H_2O_2 solution (400 mM in buffer), 100 μL of the PNPG solution (100 mM in buffer) and the total volume was brought to 1 mL with buffer. Reference tests were performed without catalyst. In all cases the total volume was brought to 1 mL with carbonate buffer. The reaction mixtures were manually stirred prior to each measurement to prevent the formation of gas bubbles in the cuvette. Quantification of the product (4-nitorophenolate) was performed by measuring the absorbance at 400 nm (ε = 1.85 × 104 M^{-1} cm^{-1}) every minute for the first 20 min, 2 h and after 24 h. Note that for the measurement after 24 h, the catalytic solution was diluted 10 times. The assays were performed at room temperature (20 °C–25 °C) protected from light.

Computations

Computations have been carried out using the Jaguar 8.5 pseudospectral program package 8 (Jaguar 8.5, Schrodinger, Inc., New York, NY, 2014). All species have been fully geometry optimized, and the Cartesian coordinates are given in the annex. Density Functional Theory (DFT) was applied by the means of the B3LYP functional[59,60] corrected for dispersion as proposed by Grimme (D3 correction).[61] The LACV3P basis set as implemented in Jaguar was used for the copper atom and the standard split valence polarized 6-31+G(d) basis set[62] was used for all other atoms. Electronic energies were obtained after corresponding fully analytical single point calculations, at the BP86/6-31+G(d) level of theory. Thermal and entropic contributions to free energy (at 298.15 K) and zero-point energy have been obtained by performing frequency calculations at the B3LYP-D3/6-31+G(d) level of theory.

Author contributions

The manuscript and the results included were prepared through contributions of all authors. All authors have given approval to the final version of the manuscript.

Data availability

The data supporting this article have been included as part of the ESI.† Further detailed synthetic descriptions, UV-Vis, EPR, electrochemical analyses, and catalytic results are provided in the ESI.† X-ray crystallographic files for **1–6** and $\mathbf{3^{Tr}}$ are provided in CIF format. CCDC 2369751–2369758† contain the supplementary crystallographic data for this paper.

Conflicts of interest

There are no conflicts to declare.

Acknowledgements

This project has received funding from the European Union's Horizon 2020 research and innovation programme under the Marie Skłodowska-Curie (H2020-MSCA-IF-2016) grant agreement no. 753953 for Y. Y. S. L., U. G. was supported through a doctoral fellowship from the Fonds de la Recherche Scientifique – FNRS (FNRS-Aspirant). X. M. was supported through a China Scholarship Council fellowship. M. B. was supported through a doctoral fellowship from the Fonds de la Recherche Scientifique – FNRS (FNRS-FRIA). Computational resources have been provided by the supercomputing facilities of the Université catholique de Louvain (CISM/UCL) and the Consortium des équipements de Calcul Intensif en Fédération

Wallonie Bruxelles (CPCI) funded by the Fonds de la Recherche Scientifique – FNRS under convention 2.5020.11. We thank the Centre d'Instrumentation & Resonance Magnétique – CIREM (Université libre de Bruxelles – ULB) for providing support and access to its infrastructure. The EPR spectrometer used in this work has been funded by the Fonds de la Recherche Scientifique – FNRS (EQP2019-35305690), Innoviris (2019-BRIDGE-5 PhotoCop) and the Fonds des plateformes (ULB).

References

1 G. Vaaje-Kolstad, D. R. Houston, A. H. K. Riemen, V. G. H. Eijsink and D. M. F. Van Aalten, *J. Biol. Chem.*, 2005, **280**, 11313–11319.
2 G. Vaaje-Kolstad, S. J. Horn, D. M. F. Van Aalten, B. Synstad and V. G. H. Eijsink, *J. Biol. Chem.*, 2005, **280**, 28492–28497.
3 P. V. Harris, D. Welner, K. C. McFarland, E. Re, J. C. N. Poulsen, K. Brown, R. Salbo, H. Ding, E. Vlasenko, S. Merino, F. Xu, J. Cherry, S. Larsen and L. Lo Leggio, *Biochemistry*, 2010, **49**, 3305–3316.
4 C. M. Phillips, W. T. Beeson, J. H. Cate and M. A. Marletta, *ACS Chem. Biol.*, 2011, **6**, 1399–1406.
5 R. J. Quinlan, M. D. Sweeney, L. Lo Leggio, H. Otten, J. C. N. Poulsen, K. S. Johansen, K. B. R. M. Krogh, C. I. Jørgensen, M. Tovborg, A. Anthonsen, T. Tryfona, C. P. Walter, P. Dupree, F. Xu, G. J. Davies and P. H. Walton, *Proc. Natl. Acad. Sci. U. S. A.*, 2011, **108**, 15079–15084.
6 G. Vaaje-Kolstad, Z. Forsberg, J. S. Loose, B. Bissaro and V. G. Eijsink, *Curr. Opin. Struct. Biol.*, 2017, **44**, 67–76.
7 S. Kim, J. Ståhlberg, M. Sandgren, R. S. Paton and G. T. Beckham, *Proc. Natl. Acad. Sci. U. S. A.*, 2014, **111**, 149–154.
8 D. M. Petrović, B. Bissaro, P. Chylenski, M. Skaugen, M. Sørlie, M. S. Jensen, F. L. Aachmann, G. Courtade, A. Várnai and V. G. H. Eijsink, *Protein Sci.*, 2018, **27**, 1636–1650.
9 D. M. Petrović, A. Várnai, M. Dimarogona, G. Mathiesen, M. Sandgren, B. Westereng and V. G. H. Eijsink, *J. Biol. Chem.*, 2019, **294**, 15068–15081.
10 E. A. Span, D. L. M. Suess, M. C. Deller, R. D. Britt and M. A. Marletta, *ACS Chem. Biol.*, 2017, **12**, 1095–1103.
11 T. Tandrup, T. Tryfona, K. E. H. Frandsen, K. S. Johansen, P. Dupree and L. Lo Leggio, *Biochemistry*, 2020, **59**, 3347–3358.
12 S. Muthuramalingam, D. Maheshwaran, M. Velusamy and R. Mayilmurugan, *J. Catal.*, 2019, **372**, 352–361.
13 A. Mendieta, J. R. Álvarez-Idaboy, V. M. Ugalde-Saldívar, M. Flores-Álamo, A. Armenta, G. Ferrer-Sueta and L. Gasque, *Inorg. Chem.*, 2023, **62**, 16677–16690.
14 A. A. Hassoon, A. Szorcsik, L. Fülöp, Z. I. Papp, N. V. May and T. Gajda, *Dalton Trans.*, 2022, **51**, 17241–17254.
15 J. Saikia, V. T. Bhat, L. R. Potnuru, A. S. Redkar, V. Agarwal and V. Ramakrishnan, *ACS Omega*, 2022, **7**, 19131–19140.
16 D. Dhar and W. B. Tolman, *J. Am. Chem. Soc.*, 2015, **137**, 1322–1329.
17 C. J. Bouchey, D. Y. Shopov, A. D. Gruen and W. B. Tolman, *ACS Omega*, 2022, **7**, 35217–35232.
18 C. Citek, J. B. Gary, E. C. Wasinger and T. D. P. Stack, *J. Am. Chem. Soc.*, 2015, **137**, 6991–6994.
19 M. Bhadra, J. Y. C. Lee, R. E. Cowley, S. Kim, M. A. Siegler, E. I. Solomon and K. D. Karlin, *J. Am. Chem. Soc.*, 2018, **140**, 9042–9045.
20 S. Kim, J. Y. Lee, R. E. Cowley, J. W. Ginsbach, M. A. Siegler, E. I. Solomon and K. D. Karlin, *J. Am. Chem. Soc.*, 2015, **137**, 2796–2799.
21 G. Y. Park, M. F. Qayyum, J. Woertink, K. O. Hodgson, B. Hedman, A. A. Narducci Sarjeant, E. I. Solomon and K. D. Karlin, *J. Am. Chem. Soc.*, 2012, **134**, 8513–8524.
22 D. E. Diaz, M. Bhadra and K. D. Karlin, *Inorg. Chem.*, 2019, **58**, 13746–13750.
23 A. Kunishita, M. Kubo, H. Sugimoto, T. Ogura, K. Sato, T. Takui and S. Itoh, *J. Am. Chem. Soc.*, 2009, **131**, 2788–2789.
24 S. Itoh, *Acc. Chem. Res.*, 2015, **48**, 2066–2074.
25 S. Muthuramalingam, K. Anandababu, M. Velusamy and R. Mayilmurugan, *Inorg. Chem.*, 2020, **59**, 5918–5928.
26 I. Castillo, A. C. Neira, E. Nordlander and E. Zeglio, *Inorg. Chim. Acta*, 2014, **422**, 152–157.
27 A. C. Neira, P. R. Martínez-Alanis, G. Aullón, M. Flores-Alamo, P. Zerón, A. Company, J. Chen, J. B. Kasper, W. R. Browne, E. Nordlander and I. Castillo, *ACS Omega*, 2019, **4**, 10729–10740.
28 A. L. Concia, M. R. Beccia, M. Orio, F. T. Ferre, M. Scarpellini, F. Biaso, B. Guigliarelli, M. Réglier and A. J. Simaan, *Inorg. Chem.*, 2017, **56**, 1023–1026.
29 R. Leblay, R. Delgadillo-Ruíz, C. Decroos, C. Hureau, M. Réglier, I. Castillo, B. Faure and A. J. Simaan, *ChemCatChem*, 2023, **15**, e202300933.
30 A. Fukatsu, Y. Morimoto, H. Sugimoto and S. Itoh, *Chem. Commun.*, 2020, **56**, 5123–5126.
31 M. G. Saulnier, D. B. Frennesson, M. D. Wittman, K. Zimmermann, U. Velaparthi, D. R. Langley, C. Struzynski, X. Sang, J. Carboni, A. Li, A. Greer, Z. Yang, P. Balimane, M. Gottardis, R. Attar and D. Vyas, *Bioorg. Med. Chem. Lett.*, 2008, **18**, 1702–1707.
32 S. Durmus, J. C. Garrison, M. J. Panzner, C. A. Tessier and W. J. Youngs, *Tetrahedron*, 2005, **61**, 97–101.
33 J. Ohkanda, J. W. Lockman, M. A. Kothare, Y. Qian, M. A. Blaskovich, S. M. Sebti and A. D. Hamilton, *J. Med. Chem.*, 2002, **45**, 177–188.
34 K. E. H. Frandsen, J. C. N. Poulsen, T. Tandrup and L. Lo Leggio, *Carbohydr. Res.*, 2017, **448**, 187–190.
35 M. Gudmundsson, S. Kim, M. Wu, T. Ishida, M. H. Momeni, G. Vaaje-Kolstad, D. Lundberg, A. Royant, J. Ståhlberg, V. G. H. Eijsink, G. T. Beckham and M. Sandgren, *J. Biol. Chem.*, 2014, **289**, 18782–18792.
36 V. V. Vu and S. T. Ngo, *Coord. Chem. Rev.*, 2018, **368**, 134–157.

37 W. A. Alves, R. H. de Almeida Santos, A. Paduan-Filho, C. C. Becerra, A. C. Borin and A. M. Da Costa Ferreira, *Inorg. Chim. Acta*, 2004, **357**, 2269–2278.
38 M. Scarpellini, A. Neves, R. Hörner, A. J. Bortoluzzi, B. Szpoganics, C. Zucco, R. A. Nome Silva, V. Drago, A. S. Mangrich, W. A. Ortiz, W. A. C. Passos, M. C. B. De Oliveira and H. Terenzi, *Inorg. Chem.*, 2003, **42**, 8353–8365.
39 A. Okuniewski, D. Rosiak, J. Chojnacki and B. Becker, *Polyhedron*, 2015, **90**, 47–57.
40 A. W. Addison, T. N. Rao, J. Reedijk, J. Van Rijn and G. C. Verschoor, *J. Chem. Soc., Dalton Trans.*, 1984, 1349–1356.
41 H. Golchoubian, O. Nazari and B. Kariuki, *J Chin. Chem. Soc.*, 2011, **58**, 60–68.
42 R. Horikoshi, Y. Funasako, T. Yajima, T. Mochida, Y. Kobayashi and H. Kageyama, *Polyhedron*, 2013, **50**, 66–74.
43 L.-S. Long, S.-P. Yang, Y.-X. Tong, Z.-W. Mao, X.-M. Chen and L.-N. Ji, *J. Chem. Soc., Dalton Trans.*, 1999, 1999–2004.
44 T. P. Mohammed, A. George, M. P. Sivaramakrishnan, P. Vadivelu, S. Balasubramanian and M. Sankaralingam, *J. Inorg. Biochem.*, 2023, **247**, 112309.
45 A. Karaliota, O. Kretsi and C. Tzougraki, *J. Inorg. Biochem.*, 2001, **84**, 33–37.
46 S. Kim, J. W. Ginsbach, J. Y. Lee, R. L. Peterson, J. J. Liu, M. A. Siegler, A. A. Sarjeant, E. I. Solomon and K. D. Karlin, *J. Am. Chem. Soc.*, 2015, **137**, 2867–2874.
47 B. Bissaro, Å. K. Røhr, G. Müller, P. Chylenski, M. Skaugen, Z. Forsberg, S. J. Horn, G. Vaaje-Kolstad and V. G. H. Eijsink, *Nat. Chem. Biol.*, 2017, **13**, 1123–1128.
48 I. Garcia-Bosch and M. A. Siegler, *Angew. Chem.*, 2016, **128**, 13065–13068.
49 M. Yamada, K. D. Karlin and S. Fukuzumi, *Chem. Sci.*, 2016, **7**, 2856–2863.
50 P. Ulanski and C. Von Sonntag, *J. Chem. Soc., Perkin Trans. 2*, 1999, 165–168.
51 G. Louit, S. Foley, J. Cabillic, H. Coffigny, F. Taran, A. Valleix, J. P. Renault and S. Pin, *Radiat. Phys. Chem.*, 2005, **72**, 119–124.
52 L. Cecilia Friedrich, C. Lúcia de Paiva e Silva Zanta, A. Machulek Jr, V. de Oliveira Silva and F. H. Quina, *Sci. Agric.*, 2012, **69**, 347–351.
53 A. N. Pham, G. Xing, C. J. Miller and T. D. Waite, *J. Catal.*, 2013, **301**, 54–64.
54 L. Cao, O. Caldararu, A. C. Rosenzweig and U. Ryde, *Angew. Chem.*, 2018, **130**, 168–172.
55 J. Ipsen, C. Hernández-Rollán, S. J. Muderspach, S. Brander, A. B. Bertelsen, P. E. Jensen, M. H. H. Nørholm, L. Lo Leggio and K. S. Johansen, *FEBS Lett.*, 2021, **595**, 1708–1720.
56 E. Chiu, M. Hijnen, R. D. Bunker, M. Boudes, C. Rajendran, K. Aizel, V. Oliéric, C. Schulze-Briese, W. Mitsuhashi, V. Young, V. K. Ward, M. Bergoin, P. Metcal and F. Coulibaly, *Proc. Natl. Acad. Sci. U. S. A.*, 2015, **112**, 3973–3978.
57 S. Garcia-Santamarina, C. Probst, R. A. Festa, C. Ding, A. D. Smith, S. E. Conklin, S. Brander, L. N. Kinch, N. V. Grishin, K. J. Franz, P. Riggs-Gelasco, L. Lo Leggio, K. S. Johansen and D. J. Thiele, *Nat. Chem. Biol.*, 2020, **16**, 337–344.
58 S. Stoll and A. Schweiger, *J. Magn. Reson.*, 2006, **178**, 42–55.
59 A. D. Becke, *J. Chem. Phys.*, 1993, **98**, 5648–5652.
60 P. J. Stephens, F. J. Devlin, C. F. Chabalowski and M. J. Frisch, *J. Phys. Chem.*, 1994, **98**, 11623–11627.
61 S. Grimme, J. Antony, S. Ehrlich and H. Krieg, *J. Phys. Chem.*, 2010, **132**, 154104.
62 W. J. Hehre and W. A. Lathan, *J. Chem. Phys.*, 1972, **56**, 5255–5257.